

Transport and Structural Properties of Pure and Cr Doped  $\text{Li}_3\text{VO}_4$ 

V. Massarotti,<sup>\*,†</sup> D. Capsoni,<sup>†</sup> M. Bini,<sup>†</sup> P. Mustarelli,<sup>†</sup> G. Chiodelli,<sup>‡</sup> C. B. Azzoni,<sup>§</sup>  
P. Galinetto,<sup>§</sup> and M. C. Mozzati<sup>§</sup>

Dipartimento di Chimica Fisica "M. Rolla" dell'Università, viale Taramelli 16, 27100 Pavia, Italy,  
CNR—IENI, Sezione di Pavia, viale Taramelli 16, 27100 Pavia, Italy, CNISM—Dipartimento di Fisica "A.  
Volta" dell'Università, via Bassi 6, 27100 Pavia, Italy

Received: March 7, 2005; In Final Form: June 17, 2005

This study deals with the effects of 5 and 10% chromium additions on the transport and structural properties of  $\text{Li}_3\text{VO}_4$ . The Cr substitution is easily obtained without impurity phases and does not affect the room- and high-temperature host crystal structure, as evidenced by X-ray powder diffraction and micro-Raman analysis. The EPR signals are interpreted in terms of quantified amounts of Cr ions in 5+ and 3+ valence states. Suitable  $^7\text{Li}$  and  $^{51}\text{V}$  MAS NMR spectra simulations agree with the EPR results about the relative amount of  $\text{Cr}^{5+}$  and  $\text{Cr}^{3+}$  ions substituted in  $\text{V}^{5+}$  and  $\text{Li}^+$  sites, respectively. The  $\text{Cr}^{3+}$  presence on Li site, also suggested by Raman results and Rietveld refinements, requires Li vacancies to maintain the charge neutrality. The p-type conductivity, suggested by the positive thermoelectric power coefficients, significantly increases by the cation doping up to an order of magnitude.

## Introduction

Lithium vanadate ( $\text{Li}_3\text{VO}_4$ ) is a material suitable for applications in the fields of optics, electrochemistry, and electronics.<sup>1</sup> For what concerns the transport properties, this compound behaves as a solid ionic-conducting electrolyte because of the high mobility of lithium ions in the structure.<sup>2–4</sup>  $\text{Li}_3\text{VO}_4$  and other isostructural compounds (e.g.,  $\text{Li}_3\text{PO}_4$ ,  $\text{Li}_3\text{AsO}_4$ ) belong to a family of solid conducting electrolytes showing high conductivity ( $\sigma$ ) in the  $\gamma$ -type form generally stable at high temperature (HT).<sup>5</sup> Song et al.<sup>3</sup> report a relatively high room-temperature (RT) conductivity for the  $\beta$ II form of both solid state and sol–gel  $\text{Li}_3\text{VO}_4$  samples.

The most studied materials for electrochemical applications, among the complex solid solutions systems, were  $\text{Li}_3(\text{P}, \text{V}, \text{As})\text{O}_4\text{--Li}_4\text{GeO}_4$ ,  $\text{Li}_3(\text{P}, \text{V}, \text{As})\text{O}_4\text{--Li}_4\text{TiO}_4$ .<sup>6</sup> A typical RT  $\sigma$  value of  $4 \cdot 10^{-5} \Omega^{-1} \text{cm}^{-1}$  was reported for the system  $\text{Li}_4\text{GeO}_4\text{--Li}_3\text{VO}_4$ ,<sup>6</sup> where the  $\gamma$ -type structure is stable in a wide temperature range. More recently, the second harmonic generation (SHG) of  $\text{Li}_3\text{VO}_4$  has been studied,<sup>7</sup> obtaining SHG coefficients comparable to those of  $\text{LiNbO}_3$ , one of the most efficient frequency doubler materials. Moreover, the recent successful research on new routes for obtaining lithium vanadate single crystals<sup>8,9</sup> allowed a great development of these applications.

The  $\text{Li}_3\text{VO}_4$  orthorhombic  $\beta$ II form (space group  $Pmn2_1$ ),<sup>10,11</sup> stable at RT, consists of an oxygen tetrahedral network.  $\text{Li}^+$  ions occupy two different crystallographic sites (Li1 and Li2), while a third cationic site is occupied by  $\text{V}^{5+}$  ions; empty sites also exist, allowing the  $\text{Li}^+$  cation migration. Other polymorphs were revealed by X-ray powder diffraction (XRPD) by increasing temperature up to the melting point; only for the  $\gamma$ II form stable at 1073 K were the diffraction peaks indexed.<sup>10</sup> The

crystallographic details<sup>11</sup> show that the  $\text{LiO}_4$  tetrahedra are larger and more distorted than those of  $\text{VO}_4$ .

This paper deals with the effect of chromium doping (up to 10% of the V-cationic fraction) on the structure and transport properties of  $\text{Li}_3\text{VO}_4$ . Indeed, the possible Cr and V isovalence and their similar ionic radii could be important conditions to reach a large composition range in the solid solutions. XRPD and micro-Raman measurements at RT were carried out to verify structure preservation and impurity absence, while the abundance of cation substitution and the valence state of the doping ions were investigated by electron paramagnetic resonance (EPR) and  $^7\text{Li}$  and  $^{51}\text{V}$  magic-angle spinning nuclear magnetic resonance (MAS NMR). Conductivity and thermopower measurements were performed in a wide temperature range to characterize the transport properties. To investigate the thermal stability of the solid solutions also, HT XRPD measurements were carried out.

## Experimental Section

$\text{Li}_3\text{VO}_4$  was prepared by solid-state synthesis from the starting mixture  $\text{Li}_2\text{CO}_3$  (Aldrich 99.6%) and  $\text{V}_2\text{O}_5$  (Aldrich 99.6%) in the proper amount.  $\text{Cr}_2\text{O}_3$  (Aldrich 99.995%) was added to the mixture to obtain 5 and 10% of vanadium atomic fraction substitution. The mixed powders were ground, pelletized, and treated in Au foil for 24 h at 1073 K, cooled in 24 h to 853 K, maintained for 24 h at 853 K, and finally slowly cooled to RT.

Disk-shaped samples were pelletized from the powders and sintered at 1073 K, reaching a densification degree higher than 96%. Platinum was evaporated and was deposited on the opposite surfaces in order to ensure good electrical contact for the conductivity measurements.

XRPD measurements were performed at RT on a Bruker D5005 diffractometer with the  $\text{Cu K}\alpha$  radiation and Ni filter to control the purity of the produced samples and their crystalline form. Structural and profile refinement by the Rietveld method was carried out by means of FULLPROF program<sup>12</sup> on the basis of the structural model proposed by Shannon and Calvo.<sup>10</sup> The

\* Corresponding Author. E-mail: vincenzo.massarotti@unipv.it. Telephone: 39-382-987203. Fax: 39-382-987575.

<sup>†</sup> Dipartimento di Chimica Fisica "M. Rolla" dell'Università.

<sup>‡</sup> CNR—IENI, Sezione di Pavia.

<sup>§</sup> CNISM, Dipartimento di Fisica "A. Volta" dell'Università.

doped samples were treated on the basis of different substitutional models, and no refinement of occupancy factors was performed.

HRPD measurements were also performed in air at different temperatures up to 1223 K and at a fixed temperature as a function of time to investigate the presence of the HT forms and their stability. The HT patterns were collected by means of an Anton Paar HTK 1200 polythermal attachment and a position-sensitive detector (PSD) able to reduce the collection time.

For the electrical characterization of the samples, impedance spectroscopy (IS) measurements were performed from 573 up to 1200 K by using a Solartron 1260 frequency response analyzer (FRA) in the frequency range  $10^{-3}$ – $10^7$  Hz, with the experimental setting described elsewhere.<sup>13</sup>

Thermoelectric power ( $\alpha$  coefficient) measurements were performed up to 1200 K by means of the electrochemical cell already described.<sup>14</sup>

Micro-Raman measurements were carried out at RT by using a Labram Dilor spectrometer equipped with an Olympus microscope HS BX40. The 632.8-nm light from a He–Ne laser was employed as excitation radiation. The samples, mounted on a motorized *xy* stage, were tested with a 100x objective and with a laser spot of  $\sim 1 \mu\text{m}$  of diameter.

X-band ( $\sim 9.4$  GHz) EPR measurements were carried out at RT. Particular care was paid in determining the sample mass and its position in the resonant cavity to compare signal intensities (areas); the signals, interpreted by numerical methods, were resolved in their different components, whose areas were determined with an error of about 10%.

NMR measurements were performed at RT on a AMX400WB spectrometer (Bruker) based on a 9.4 T magnet. MAS spectra were acquired with a 4-mm probehead (Bruker), equipped with cylindrical zirconia rotors and a boron nitride stator.  $^{51}\text{V}$  MAS NMR spectra were collected at 105.19 MHz. The samples were spun at 12 kHz, and the data were averaged over 12k acquisitions using a single-pulse sequence, with a  $15^\circ$  pulse of  $0.5 \mu\text{s}$ , a recycle time of 1 s, and a spectral width of 900 kHz. The baseline distortions were corrected by linear prediction of the first 10–15 points of the FIDs, followed by baseline correction (software WINNMR, Bruker). The simulations of the spectra were performed by using the WSOLIDS package.<sup>15</sup>  $^7\text{Li}$  MAS NMR measurements were performed at 155.6 MHz. The samples were spun at 10 kHz, and the data were averaged over 32 acquisitions using a single-pulse sequence, with a  $90^\circ$  pulse of  $3 \mu\text{s}$  and a recycle time of 10 s. The spectra were referenced to an external sample of 1.0 M LiCl in  $\text{H}_2\text{O}$ .

## Results

**HRPD.** At RT, both pure and doped samples showed the only lines pertinent to the orthorhombic  $Pmn2_1$  form ( $\beta$ II) of  $\text{Li}_3\text{VO}_4$  reported in the literature,<sup>10</sup> except for some discrepancies on peak intensities due to preferred orientation effects for  $0k0$  planes. The Rietveld structural refinement of the sample patterns was carried out. For doped samples, different substitutional models concerning the Cr distribution on the three cationic sites were tested. The lowest values of the  $\chi^2$  agreement factor<sup>12</sup> suggest the reliability of the model on the basis of the Cr substitution on V site; the pertinent results are reported in Table 1. From the refined values of lattice parameters and atomic coordinates, the bond lengths were evaluated and reported in Table 2 for the first, second, and third coordination. However, different cationic distributions with a small Cr amount on Li

**TABLE 1: Lattice Parameters and Discrepancy Factors Obtained from Rietveld Refinement**

	pure	Cr 5%	Cr 10%
$a$ , Å	6.3253(1)	6.3250(1)	6.3247(1)
$b$ , Å	5.4464(1)	5.4457(1)	5.4448(1)
$c$ , Å	4.9476(1)	4.9475(1)	4.9478(1)
$R_{\text{wp}}$	11.6	10.9	11.4
$\chi^2$	1.91	1.60	1.72
$R_B$	7.33	5.44	6.24

**TABLE 2: Number and Distances of First, Second, and Third Coordination Shell for Cationic Sites**

central atom	bonded atom	bond length (Å)
Li1	$2 \times \text{O1}$	2.027, 2.014
	O2	1.928
	O3	1.972
	$4 \times \text{Li1}$	$2 \times 3.112, 3.275, 3.050$
	$4 \times \text{Li2}$	3.227, 3.129, 3.087, 2.996
	$4 \times \text{V}$	3.136, 3.107, 3.049, 3.126
Li2	$6 \times \text{Li1}$	$2 \times 4.338, 4 \times 4.435$
	$2 \times \text{O1}$	$2 \times 1.994$
	O2	2.092
	O3	1.951
	$8 \times \text{Li1}$	$2 \times 3.227, 2 \times 3.129, 2 \times 2.995, 2 \times 3.087$
	$4 \times \text{V}$	$2 \times 3.164, 2.982, 3.150$
V	$4 \times \text{Li2}$	$4 \times 4.388$
	$2 \times \text{V}$	4.339, 4.456
	$2 \times \text{O1}$	$2 \times 1.677$
	O2	1.689
	O3	1.705
	$8 \times \text{Li1}$	$2 \times 3.135, 2 \times 3.107, 2 \times 3.049, 2 \times 3.126$
	$4 \times \text{Li2}$	$2 \times 3.164, 2.982, 3.150$
	$2 \times \text{Li2}$	4.339, 4.456
	$4 \times \text{V}$	$4 \times 4.421$

sites can be also considered reliable ( $\chi^2 = 1.94$  and 2.09 for Cr 5% and Cr 10% samples, respectively).

From HT measurements, all the samples evidenced, in the 993–1033 K and 1033–1073 K intervals, two structural transitions, reversible as confirmed by RT measurements after the thermal cycle. As an example, in Figure 1, the diffraction patterns for the Cr 5% doped sample are reported. In pure  $\text{Li}_3\text{VO}_4$ , a remarkable peak intensity change between the initial RT pattern and that collected after the thermal cycle is observed; the difference is removed after grinding (Figure 2).

The patterns collected vs time at 1033 K show an evolution toward the final form in about 9 h for the pure sample, a time

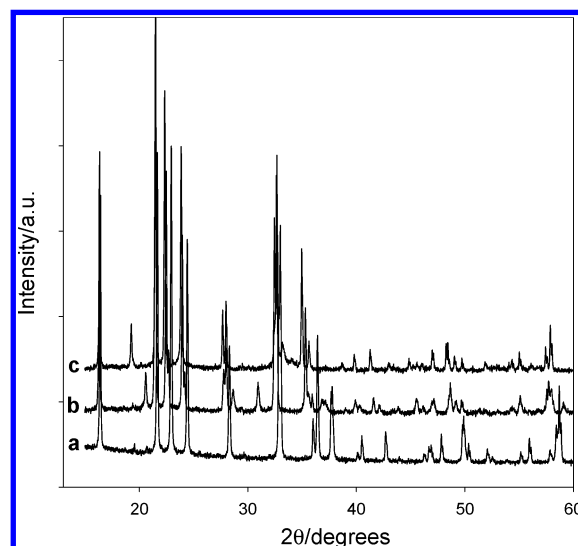


**Figure 1.** XRPD patterns of Cr 5% doped sample collected at (a) RT, (b) 1033 K, and (c) 1113 K.

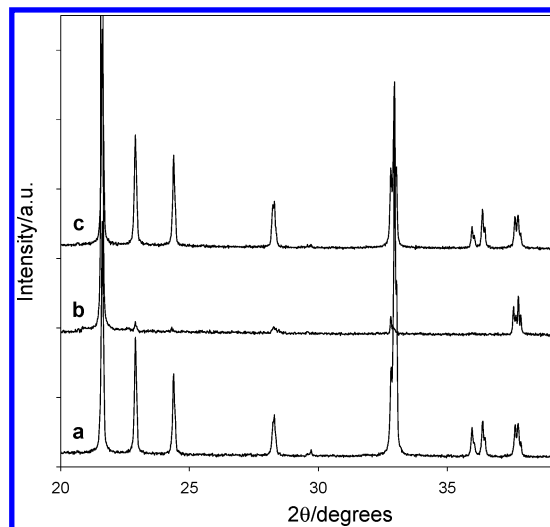


**Figure 2.** XRPD patterns of pure  $\text{Li}_3\text{VO}_4$  collected at RT (a) before the thermal cycle and (b) and (c) after the thermal cycle up to 1113 K without and with grinding, respectively.

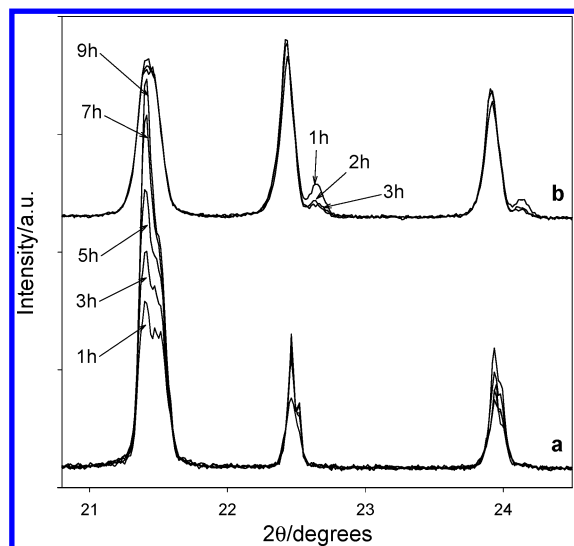


**Figure 3.** Comparison between the XRPD patterns at 1033 K vs time for (a) pure  $\text{Li}_3\text{VO}_4$  and (b) Cr 5% doped sample.

much greater than that of doped samples (2 h); in Figure 3 the comparison between the pure and the Cr 5% doped sample is reported. A faster recovery in doped samples was also observed at 1113 K for the upper transition.

Indexing processes have been carried out to characterize the HT forms in the Cr 5% doped sample; no satisfactory results were obtained on the first HT phase, while the second HT phase was explained with the  $\gamma$ II form.<sup>16</sup> Crystal data pertinent to the same phase are reported also in the JCPDS database (24-0666 card number). The least-squares refinement of orthorhombic lattice parameters leads to  $a = 11.0601(36)$  Å,  $b = 6.4445(21)$  Å, and  $c = 5.1795(17)$  Å.

**Impedance Spectroscopy and Conductivity.** All the samples show similar impedance plots, consisting of a half circle coming out of the origin due to the bulk contribution, followed by an initial arc related to electrode reaction. As an example, the IS results at 623 K on pure, Cr 5%, and Cr 10% samples are reported in Figure 4. The grain boundary contribution is absent. The bulk resistivity decreases significantly with increasing the dopant percentage.

The Arrhenius plots of pure, Cr 5% and Cr 10% doped samples are reported in Figure 5a and compared with some

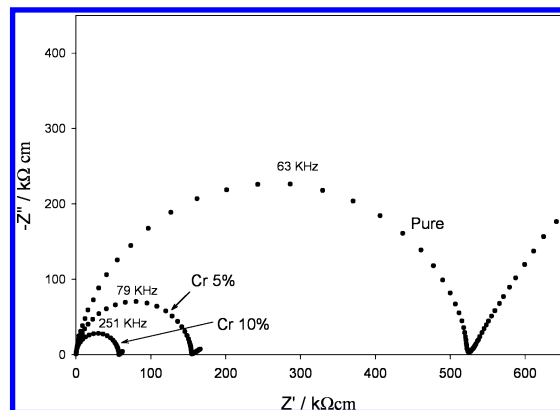


**Figure 4.** Impedance plots of pure and doped samples at 623 K.

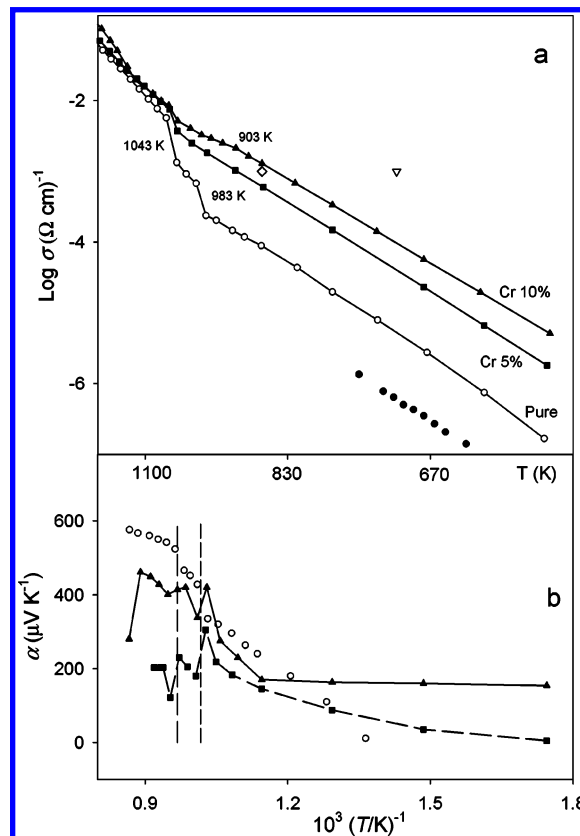


**Figure 5.** (a) Arrhenius plots and (b) thermoelectric power ( $\alpha$ ) of pure and doped samples. In (a) Mishra et al.<sup>2</sup> (down triangle), Song et al.<sup>3</sup> (open diamond), and single-crystal data<sup>8</sup> (full circle) are also reported.

literature results for pure  $\text{Li}_3\text{VO}_4$ .<sup>2,3</sup> The pure sample shows two discontinuities at about 983 and 1043 K. The doped samples show only the discontinuity at higher temperature, less evident than for the pure sample, their conductivity being higher in the lower temperature region. In the  $T > 1073$  K region, the conductivity is practically independent of doping.

The thermoelectric power coefficients  $\alpha$ , reported in Figure 5b, evidence positive values for all the samples but different behaviors with increasing temperature. Jumps at the structural transitions (about 983 and 1043 K) are evidenced.

**Micro-Raman Spectroscopy.** The micro-Raman spectra of the pure and doped samples are reported in Figure 6. The main Raman peaks, due to vibrations of  $\text{VO}_4$  tetrahedra, appear at  $\sim 793$  and  $\sim 826$   $\text{cm}^{-1}$ , in very good agreement with previously reported Raman spectra of  $\text{Li}_3\text{VO}_4$  single crystals.<sup>8</sup> In the lower-energy part of the spectra, magnified in Figure 6, well-defined Raman modes are observed for the pure sample at  $\sim 338$ , 358,

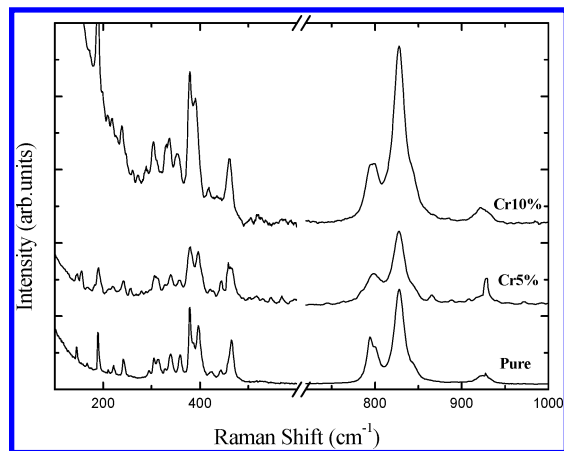


**Figure 6.** Raman spectra at RT of pure and doped samples. The data in the range 150–600 cm<sup>-1</sup> are multiplied by 3 with respect to the data at higher energy.

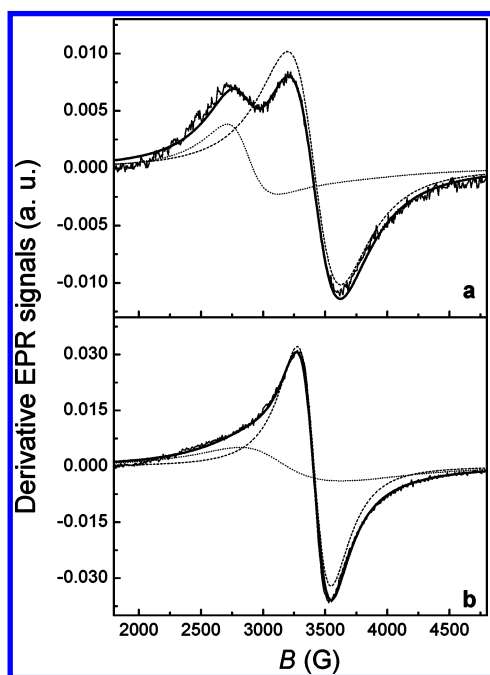


**Figure 7.** EPR spectra (thin solid line) compared with their numerical simulation (thick solid line) of (a) Cr 5% and (b) Cr 10% doped samples. The symmetric (dashed line) and the asymmetric component (dotted line) of the simulated spectra are also shown.

379, 396, and 465 cm<sup>-1</sup>. No Raman structures are present in the region 600–750 cm<sup>-1</sup>, omitted in Figure 6 for sake of simplicity. The doping does not introduce new intense Raman modes, and no impurity phases can be detected.

**EPR.** No EPR signals were evidenced in the pure sample. Figure 7 shows the signals at RT for Cr 5% and Cr 10% doped samples. In both cases, the signal can be interpreted as a sum of a symmetric and an asymmetric component. The whole signal area of Cr 10% sample is practically twice of that of the Cr 5% sample, so proving that the signal is completely due to Cr ions.

The symmetric component centered at 3408 G ( $g = 1.97$ ) shows a Lorentzian shape and a line width ( $\Delta B$ ) of 270 G in the Cr 10% sample and 425 G in the Cr 5% sample. It can be attributed to Cr<sup>5+</sup> ( $d^1$ ,  $L = 2$ ,  $S = 1/2$ ) in a slightly distorted tetrahedral coordination (as for V<sup>5+</sup> site). Indeed, by assuming a trigonal quantization axis, as suggested from oxygen coordinates and by crystal field (CF)<sup>17</sup> calculation, the ground state for Cr<sup>5+</sup> results to be, for  $\lambda = 0$ , the orbital singlet (terms with

negligible coefficients are omitted)

$$0.27|-2\rangle + 0.65|1\rangle + 0.27|2\rangle - 0.65|-1\rangle$$

Such a spin doublet should give rise to an isotropic EPR signal with  $g = 2$ . Taking into account a mixing with upper states resulting from the spin–orbit interaction ( $\lambda < 100$  cm<sup>-1</sup>), the EPR signal will be slightly anisotropic with a mean  $g$  value  $< 2$ , in agreement with the experimental signal, for which, anyway, the anisotropy is not evident because of the very similar  $g_x$ ,  $g_y$ ,  $g_z$ , and the large  $\Delta B$  value, and also in agreement with literature results for single crystals.<sup>18</sup>

The asymmetric component is different for the two samples. The numerical analysis suggests for the Cr 10% sample a signal with the following parallel (p) and orthogonal (o) signal parameters:  $g_p = 1.77$ ,  $\Delta B_p = 900$  G and  $g_o = 2.2$ ,  $\Delta B_o = 600$  G, while for the Cr 5% sample, the values  $g_p = 1.77$ ,  $\Delta B_p = 900$  G and  $g_o = 2.35$ ,  $\Delta B_o = 300$  G are found. This component can be attributed to Cr<sup>3+</sup> ion ( $d^3$ ,  $L = 3$ ,  $S = 3/2$ ) in distorted tetrahedral sites and with an orbital singlet ground state, resulting from a linear combination of the degenerate states

$$\pm\sqrt{5/6}|\mp 2\rangle + \sqrt{1/6}|\pm 1\rangle$$

for  $\lambda = 0$ ,<sup>19</sup> split by the distortion of the tetrahedral coordination. This state, with spin multiplicity four, should give rise to an anisotropic EPR signal with  $g_x$ ,  $g_y = g_o = 4$  and  $g_z = g_p = 2$ . The spin–orbit interaction strongly modifies the ground-state coefficients and the related  $g$  values fitting the experimental data. The different  $g_o$  values for the two samples suggest the possible insertion of Cr<sup>3+</sup> also in sites different from the V one, possibly Li sites.

For the Cr 5% sample the calculated area ratio of the isotropic and anisotropic components is  $\sim 2.5$ , while for the Cr 10% sample, it is  $\sim 1.4$ .

**MAS NMR.** Figure 8 shows the <sup>7</sup>Li MAS NMR spectra of all the samples. The spectrum of pure Li<sub>3</sub>VO<sub>4</sub> is characterized by a single Gaussian peak at  $\sim 0$  ppm, with full width at half-height (fwhh) of about 760 Hz. The addition of chromium leads to the growth of two peaks with paramagnetic shifts of 46 and 55 ppm, whose combined intensity is well related with the doping amount. The relative intensities (areas) are reported in Table 3. Similar features were observed in defective LiMn<sub>2</sub>O<sub>4</sub> spinels by means of both <sup>6</sup>Li and <sup>7</sup>Li MAS.<sup>20</sup>

Figure 9 shows the <sup>51</sup>V ( $I = 7/2$ ) MAS NMR spectra of the central and satellite transitions of all the samples. For each sample, the insets show the spectral region of the isotropic peaks (lower), together with their simulations (upper). Pyro- ortho- and metavanadates have been deeply studied for their application in catalysis.<sup>21–25</sup> In particular, the <sup>51</sup>V spectra of orthovanadates are characterized by small chemical shift anisotropies. Therefore, the spectrum of pure Li<sub>3</sub>VO<sub>4</sub> was simulated in terms of a single site by using the quadrupolar parameters reported by Lapina et al.<sup>21</sup> ( $Q_{cc} = 1.53$  MHz,  $\eta_Q = 0.05$ ), which gave a RMS error  $< 0.5\%$ . A sensitivity study performed starting from the single-crystal parameters recently reported by Lim et al.<sup>26</sup> ( $Q_{cc} = 1.44$  MHz,  $\eta_Q = 0$ ), showed differences in the range 0.1–0.5%. The spectra of Cr 5% and Cr 10% doped samples were simulated with a three-site model by imposing the quadrupolar parameters of pure Li<sub>3</sub>VO<sub>4</sub> to the main site (undisturbed vanadium). The two additional sites were assigned to <sup>51</sup>V nuclei perturbed by Cr doping, as suggested by parallel EPR findings (see discussion). The combined intensities of sites 2 and 3 accounted for  $\sim 26\%$  ( $18\% + 8\%$ ) and  $\sim 42\%$  ( $26\% + 16\%$ ) in the case of 5% and 10% doping, respectively. The combined use of different spectroscopic techniques makes more reliable the results of our



**TABLE 3: Parameters of  $^7\text{Li}$  MAS NMR Spectra**

sample	site 1			site 2			site 3		
	c.s. (ppm)	intensity (%)	fwhh (Hz)	c.s. (ppm)	intensity (%)	fwhh (Hz)	c.s. (ppm)	intensity (%)	fwhh (Hz)
pure	0.3	100	760						
Cr 5%	0.3	94.9	680	46	2.5	~650	55	2.6	~650
Cr 10%	0.3	91.8	680	46	4.1	~650	55	4.1	~650

fitting procedure that, per se, are not unique. In fact, a large part of the information on the quadrupolar parameters is carried by the spinning sidebands manifold, which was not simulated here. This is particularly relevant in the case of quite featureless peaks as those reported in Figure 9.

### Discussion

XRPD results at RT indicate the same structure for the pure<sup>10</sup> and doped samples, the chromium substitution leaving the lattice parameters substantially unaffected (see Table 1). The refined structural results (see Table 2) show that the most compact  $\text{VO}_4$  tetrahedra are more regular than the most enlarged and distorted  $\text{Li}_2\text{O}_4$  and  $\text{LiIO}_4$ . The transition temperature and the related crystal phase do not depend on the dopant amount, pointing out a substantial thermodynamic stability of the HT forms. On the other hand, the Cr substitution allows obtaining of the HT forms in less time with respect to the pure sample (Figure 3) and removes the strain and preferred orientation effects observed in the pure  $\text{Li}_3\text{VO}_4$  after the thermal cycle (Figure 2). So, Cr doping influences both kinetic and microstructural aspects of the transitions.

Our conductivity measurements well evidence the doping effect in the temperature range 573–1073 K: the doped samples show  $\sigma$  values greater than the pure one (see Figure 5a) up to an order of magnitude greater for Cr 10% and show the only structural transition at 1043 K. The two phase transitions are,

anyway, detectable in the doped samples from both XRPD measurements (Figure 1) and the thermoelectric power data (Figure 5b). Previously reported  $\text{Li}_3\text{VO}_4$   $\sigma$  values<sup>2,3</sup> are remarkably greater than our pure sample values and comparable with those of our doped samples, indicating possible impurity effects in the literature compounds. Also, the RT  $\sigma$  value ( $1.71 \cdot 10^{-5} \Omega^{-1} \text{cm}^{-1}$ ) for  $\text{Li}_3\text{VO}_4$  from solid-state synthesis<sup>3</sup> is surprisingly high for the insulating  $\beta\text{II}$  phase; according to our trend, a significantly lower  $\sigma$  value (at least 6 orders of magnitude) is expected at RT. On the contrary, single-crystal  $\sigma$  values<sup>8</sup> show a trend vs  $1/T$  ( $E_a = 0.85$  eV) in the range 670–743 K, very similar with respect to our data ( $E_a = 0.87$  eV), even if the absolute  $\sigma$  values are lower by about 1 order of magnitude. Such conductivity values are pertinent to a particular direction because of the cut of a crystal slab perpendicular to the  $a$  axis.

For the pure sample, the  $\alpha$  value increases with increasing temperature. This behavior is less evident in the doped samples, so suggesting a higher stabilization of charge carrier concentration: the  $\alpha$  value of the Cr 10% sample is nearly constant from RT up to ~900 K. However, the  $\alpha$  values are positive, related

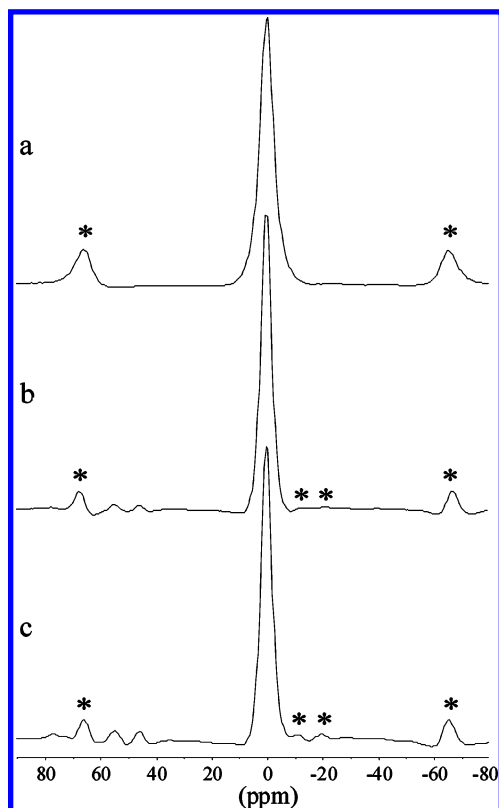


**Figure 8.**  $^7\text{Li}$  MAS NMR spectra of (a) pure, (b) Cr 5%, and (c) Cr 10% samples. The stars mark the spinning sidebands.

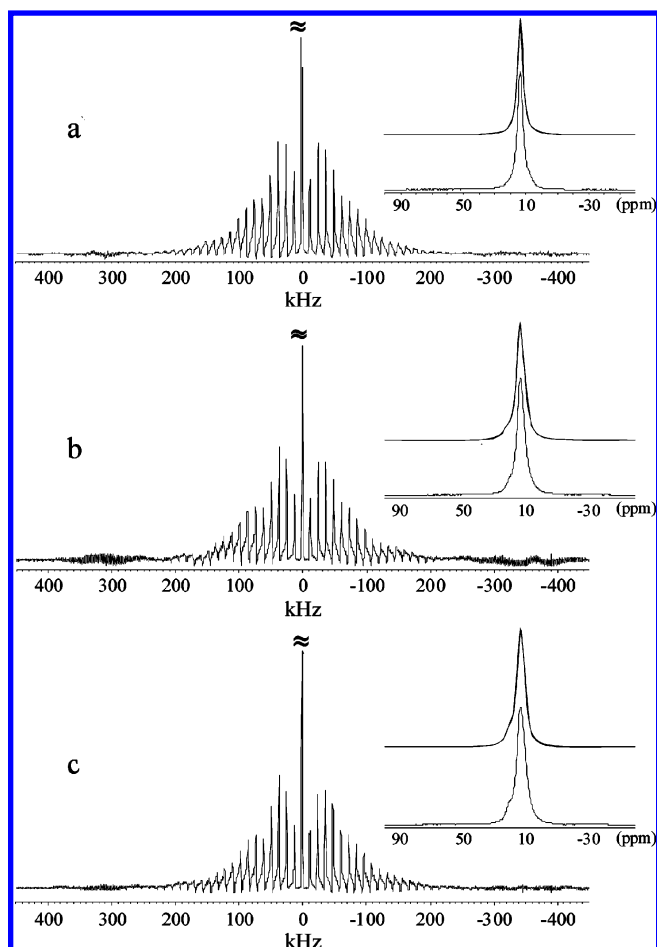


**Figure 9.**  $^{51}\text{V}$  MAS NMR spectra of the central and satellite transitions of (a) pure, (b) Cr 5%, and (c) Cr 10% samples. For each sample, the insets show the spectral region of the isotropic peaks (lower), together with their simulations (upper).

with the positive sign of charge carriers, in agreement with other results on pure  $\text{Li}_3\text{VO}_4$ .<sup>2</sup> On the basis of the possible Frenkel defect in the lithium sublattice, it can be assumed that the increase of vacancy concentration, related to a substitutional defect ( $\text{Cr}^{3+}$  on  $\text{Li}^+$ ), implies a corresponding decrease of interstitial Li ions. So, the increase of both conductivity and  $\alpha$  values at any  $T$  for  $T < 770$  K can be explained by the vacancy concentration increase related to the dopant amount.

The Raman spectrum of pure  $\text{Li}_3\text{VO}_4$  has been poorly studied previously. Despite its orthorhombic form and space group  $Pmn2_1$ , the  $\text{Li}_3\text{VO}_4$  Raman features can be better understood, taking into account separately the vibrations involving the  $\text{LiO}_4$  tetrahedral group, giving rise usually to Raman modes below  $500\text{ cm}^{-1}$ , and the  $\text{VO}_4$  group. Concerning the  $\text{VO}_4$  group vibrations, we can take as a comparison  $\text{LiNiVO}_4$ ,<sup>27</sup> having cubic spinel structure with  $Fd3m$  (Oh7) symmetry and for which the strongest Raman lines, associated with stretching vibrations, are just observed at  $790$  and  $823\text{ cm}^{-1}$  as for our samples. The bending mode, responsible for the signal at  $337\text{ cm}^{-1}$ , is also present in our spectra. In the lower-energy region, several less-intense Raman features are observable. These signals are probably due to the couplings between some of the above-mentioned vibrations.<sup>28</sup>

In the Raman spectra of doped samples, no new peaks can be observed with respect to the  $\text{Li}_3\text{VO}_4$  one, except very low ones around  $500\text{ cm}^{-1}$ . Some differences can be observed in the doublet around  $400\text{ cm}^{-1}$ ; the splitting between the two peaks decreases from  $17$  to  $10\text{ cm}^{-1}$ , passing from the pure to the Cr 10% sample, so suggesting that the Cr doping influences the vibrations of Li tetrahedra. Concerning the peaks caused by the  $\text{VO}_4$  internal stretching vibrations, we notice the strict coincidence of their energies with those reported by Chitra et al.;<sup>27</sup> the frequencies and the relative intensities of these modes are not influenced by Cr substitution, and one can only observe a moderate broadening ascribable to distortions arising in the  $\text{VO}_4$  unit (see Table 2), not able in any case to modify the symmetries of the main vibrations.

The combined analysis of NMR and EPR results allows us to obtain a deeper understanding of the results of chromium substitution. As previously stated, the addition of chromium affects both the  $^{51}\text{V}$  and the  $^7\text{Li}$  NMR signals. In the case of  $^{51}\text{V}$ , two perturbed sites are found whose overall intensities scale roughly with the amount of doping. The intensity ratios of the sites are  $\sim 2.3$  for Cr 5% and  $\sim 1.6$  for Cr 10%, in good agreement with the ratios of the isotropic and anisotropic components of the EPR signals ( $\sim 2.5$  and  $\sim 1.4$ , respectively). Therefore, we can assign the NMR sites 2 and 3 to vanadium perturbed by  $\text{Cr}^{5+}$  and  $\text{Cr}^{3+}$ , respectively.

As suggested by Rietveld refinement of the XRPD patterns,  $\text{Cr}^{5+}$  mainly substitutes  $\text{V}^{5+}$  in its tetrahedral site. On the other hand, this is reasonable because of their very similar average ionic radii ( $\sim 0.35\text{--}0.40\text{ \AA}$ ). To estimate how many  $\text{V}^{5+}$  atoms will be perturbed by each  $\text{Cr}^{5+}$  substitution, we need to analyze the local structure and the connectivity of the different sites (see Table 2). Vanadium tetrahedra do not share edges or corners, but are separated by Li1- and Li2-based tetrahedra with a multiplicity 2:1. Each vanadium sees four other V atoms in the 2nd coordination shell at about  $4.42\text{ \AA}$ . On the basis of the ratios determined by EPR, the Cr 5% and Cr 10% doped samples will have  $\sim 3.6\%$  and  $\sim 5.9\%$  of  $\text{Cr}^{5+}$  in the V-sites, which will give an amount of  $\sim 14.5\%$  and  $\sim 23.6\%$  perturbed V atoms, respectively, in reasonable agreement with the NMR values (18% and 26%, respectively).

Site 3, observed in the  $^{51}\text{V}$  NMR spectra, therefore, must be assigned to the V atoms perturbed by  $\text{Cr}^{3+}$  defects. A question arises concerning the position occupied by  $\text{Cr}^{3+}$  ions in the  $\text{Li}_3\text{VO}_4$  structure. Because of its large ionic radius ( $\sim 0.68\text{ \AA}$ ), a substitution on a V site is unlikely. In contrast, it seems probable that the substitution takes place in one or both of the Li1 and Li2 sites ( $\text{Li}^+$  ionic radius  $\sim 0.6\text{ \AA}$ ), as also suggested by the different values of  $g_0$  and  $\Delta B_0$  of the anisotropic component of the EPR signals and by the changes observed around  $400\text{ cm}^{-1}$  in the Raman spectra of doped samples. Information on this point can be obtained by the  $^7\text{Li}$  NMR spectra, namely by considering the two small features observed at 46 and 55 ppm.  $\text{Cr}^{3+}$  has the same electronic structure of  $\text{Mn}^{4+}$ , whose effects on the  $^6\text{Li}$  and  $^7\text{Li}$  NMR signals have been carefully investigated.<sup>21,29</sup> The paramagnetic shift of lithium in oxide materials containing  $\text{Mn}^{4+}$  is generally caused by hyperfine Fermi-contact interaction, which is due to the unpaired electrons spin-density transfer from the paramagnet (Mn) to the NMR active spin (Li) through the Li–O–Mn bonds. The isotropic part of the interaction is given by

$$H_{\text{FC}} = I_z A \langle S_z \rangle$$

where  $A$  is the hyperfine coupling constant, and  $\langle S_z \rangle$  is the thermally averaged value of the paramagnetic spin. The value and the sign of  $A$ , which determine the entity and the direction of the shift, respectively, are related to the geometry of the Li–O–Mn bonds. In the case of the rock-salt compound  $\text{Li}_2\text{MnO}_3$ , it was shown<sup>21</sup> that each bent ( $90^\circ$ ) Li–O–Mn bond accounts roughly for 150 ppm of paramagnetic shift, while linear ( $180^\circ$ ) Li–O–Mn bonds contribute a diamagnetic shift of about  $-75$  ppm. Bent ( $120^\circ$ ) Li–O–Mn bonds in  $\text{Li}_4\text{Mn}_5\text{O}_{12}$  and  $\text{Li}_2\text{Mn}_4\text{O}_9$  spinels contribute each a  $+62$  ppm shift to the normal 8a site of lithium. The two peaks at 46 and 55 ppm in Figure 8 may be attributed to lithium in Li1 and Li2 sites perturbed by a common  $\text{Cr}^{3+}$ -substituted center. Because the areas of the two peaks are nearly the same, the chromium substitution likely takes place in the Li1 site, which is the only cation crystallographic position seeing the same number (4) of Li1 and Li2 tetrahedra in its first coordination shell (see Table 2). The average bond angles Li1–O–Li1 and Li1–O–Li2 are  $\sim 104.8^\circ$  and  $\sim 101.4^\circ$ , respectively. If we consider that the Li1–Li1 and Li1–Li2 distances are 10–15% greater than the Li–Mn ones in rock salt compounds,<sup>29</sup> the shifts observed in Figure 8 are compatible with the same through-bonds Fermi-contact mechanism observed in  $\text{Mn}^{4+}$ -rich compounds, and the peak at 46 ppm can be attributed to the lithium in the Li1 site (because of the greater bond angle). As already stated, the Li1 site sees 4 Li1 and 4 Li2 in its second coordination shell; therefore, we should expect an overall perturbed area of the peaks at 46 and 55 ppm, which is roughly four times the percentage of  $\text{Cr}^{3+}$  defects. This is true for the Cr 5% sample, where we find a  $\sim 5\%$  of perturbed Li against  $\sim 1.4\%$  of  $\text{Cr}^{3+}$  defects given by the EPR analysis. In the case of Cr 10% sample, in contrast, the fraction of perturbed Li atoms is less than expected ( $\sim 8\%$  vs an expected value of  $\sim 16\%$ , suggested by the Cr 10% EPR results). This can be explained by invoking a nonhomogeneous distribution (clustering) of the  $\text{Cr}^{3+}$  defects, possibly related to the higher  $\Delta B_0$  value of the Cr 10% EPR signal. Under the hypothesis that  $\text{Cr}^{3+}$  ions occupy the Li1 sites, the effects observed on the  $^{51}\text{V}$  spectra can be finally rationalized. Each Li1 site sees directly 4 V-based tetrahedra, and the intensities of the site 3 are in good agreement with those expected from the EPR results.

## Conclusions

In the present study, XRPD and micro-Raman analyses demonstrate that Cr ions can easily substitute on the cationic sites of the lithium vanadate structure, at least up to 10% of cation fraction, without evidence of impurity phases. The host crystal structure remains unchanged concerning both the symmetry and the lattice parameters values. Also the high-temperature polymorph structures and their transition temperatures do not depend on Cr-doping.

The EPR spectra put into evidence the presence of chromium valence states  $5+$  and  $3+$ . The combined analysis of EPR and  $^7\text{Li}$  and  $^{51}\text{V}$  MAS NMR signals allows detection that  $\text{Cr}^{5+}$  and  $\text{Cr}^{3+}$  substitute on  $\text{V}^{5+}$  and  $\text{Li}^{1+}$  crystallographic sites, respectively. The  $\text{Cr}^{3+}$  presence on the Li1 site, compatible with Rietveld refinements and Raman results, should be balanced by Li vacancies. This fact reflects on the conducting behavior of the doped samples: the greatest Cr amount with consequent highest vacancy concentration leads to the highest conductivity value. The transport mechanism is fulfilled by positive carrier movement, as suggested by the positive Seebeck coefficient values from thermoelectric power measurements.

**Acknowledgment.** This work has been partially supported by Italian Grant FIRB RBNE01KZ94.

## References and Notes

- (1) Sakata, S.; Ueda, N.; Fujii, I.; Kawazoe, H. *J. Non-Cryst. Solids* **1994**, *178*, 98.
- (2) Mishra, K. M.; Lal, A. K.; Hacque, F. Z. *Solid State Ionics* **2004**, *167*, 137.
- (3) Song, X.; Jia, M.; Chen, R. *J. Mater. Process. Technol.* **2002**, *120*, 21.
- (4) Lal, H. B.; Gaur, K.; Pathak, A. J. *J. Phys. D: Appl. Phys.* **1989**, *22*, 305.
- (5) Rodger, A. R.; Kuwano, J.; West, A. R. *Solid State Ionics* **1985**, *15*, 185.
- (6) Kuwano, J.; West, A. R. *Mater. Res. Bull.* **1980**, *15*, 1661.
- (7) Sakata, S.; Nagoshi, Y.; Nii, H.; Ueda, N.; Kawazoe, H. *J. Appl. Phys.* **1996**, *80*, 3668.
- (8) Kim, D. J.; Jun, B. E.; Kim, C.; Kim, H. K.; Kim, J. N.; Hwang, Y. *J. Appl. Phys.* **2003**, *93*, 1697.
- (9) Itoyama, W.; Iishi, K.; Sakata, S. *J. Cryst. Growth*, **1996**, *158*, 534.
- (10) West, A. R.; Glasser, F. P. *J. Solid State Chem.* **1972**, *4*, 20.
- (11) Shannon, R. D.; Calvo, C. *J. Solid State Chem.* **1973**, *6*, 538.
- (12) Rodriguez Carvajal, J.; *Physica B* **1993**, *192*, 55.
- (13) Chiodelli, G.; Massarotti, V.; Capsoni, D.; Bini, M.; Azzoni, C. B.; Mozzati, M. C.; Lupotto, P. *Solid State Commun.* **2004**, *132*, 241.
- (14) Chiodelli, G.; Flor, G.; Scagliotti, M. *Solid State Ionics* **1996**, *91*, 109.
- (15) WSOLIDS package was provided by K. Eichele. See: <http://casgm3.anorg.chemie.uni-tuebingen.de/klaus/soft/index.html>
- (16) Abrahams, I.; Bruce, P. G.; David, W. I. F.; West, A. R. *J. Solid State Chem.* **1994**, *110*, 243 and references therein.
- (17) Mozzati, M. C.; Azzoni, C. B.; Capsoni, D.; Bini, M.; Massarotti, V. *J. Phys.: Condens. Matter* **2003**, *15*, 7365.
- (18) Greenblatt, M.; Pifer, J. H. *J. Chem. Phys.* **1979**, *70*, 116.
- (19) Abragam, A.; Bleaney, B. In *Electron Paramagnetic Resonance of Transition Ions*; Clarendon Press: Oxford, 1970; p 372.
- (20) Lee, Y. J.; Wang, F.; Grey, C. P. *J. Am. Chem. Soc.* **1998**, *120*, 12601.
- (21) Skibsted, J.; Jakobsen, C. J. H.; Jakobsen, H. J. *Inorg. Chem.* **1998**, *37*, 3083.
- (22) Lapina, O. B.; Mastikhin, V. M.; Shubin, A. A.; Krasilnikov, V. N.; Zamaraev, K. I. In *Progress in NMR Spectroscopy*; Pergamon Press: London, 1992; Vol. 24, p 457.
- (23) Nielsel, U. G.; Jakobsen, H. J.; Skibsted, J. *Inorg. Chem.* **2000**, *39*, 2135.
- (24) Nielsel, U. G.; Jakobsen, H. J.; Skibsted, J. *J. Phys. Chem. B*, **2001**, *105*, 420.
- (25) Nielsen, U. G.; Boisen, A.; Brorson, M.; Jakobsen, C. J. H.; Jakobsen, H. J.; Skibsted, J. *Inorg. Chem.* **2002**, *41*, 6432.
- (26) Lim, A. R.; Park, S. H.; Kim, J. N.; Jang, M. S. *J. Phys. Soc. Jpn.* **2003**, *72*, 419.
- (27) Chitra, S.; Kalyani, P.; Yebka, B.; Mohan, T.; Haro-Poniatowski, E.; Gangadharan, R.; Julien, C. *Mater. Chem. Phys.* **2000**, *65*, 32.
- (28) Julien, C.; Massot, M.; Perez-Vicente, C. *Mater. Sci. Eng., B* **2000**, *75*, 6.
- (29) Mustarelli, P.; Massarotti, V.; Bini, M.; Capsoni, D. *Phys. Rev. B* **1997**, *55*, 12018.